Chinese Chemical Letters 37 (2026) 112623

Contents lists available at ScienceDirect

Chinese Chemical Letters

journal homepage: www.elsevier.com/locate/cclet

Towards equilateral triangular lattice frustrated quantum magnets through crystal symmetry–protected molecular-brick chemical strategy

Ruixin Guo[a,b,c], Jieming Sheng[e], Bowen Li[a], Kaizhen Guo[f,g], Wenjiao Yao[h], Nan Zhao[a], Jianqiao Wang[a,c], Zhibin Qiu[a,c], Bo Wen[i], Shuang Jia[f,g], Xiaoyang Wang[b], Ping Wu[a,c], Feng Yang[a], Liusuo Wu[a], Qiushi Yao[d,*], Shu Guo[a,c,*]

[a] *Shenzhen Institute for Quantum Science and Engineering, Department of Chemistry, and Department of Physics, Southern University of Science and Technology, Shenzhen 518055, China*
[b] *Beijing Center for Crystal Research and Development, Key Laboratory of Functional Crystals and Laser Technology, Technical Institute of Physics and Chemistry, Chinese Academy of Sciences, Beijing 100190, China*
[c] *International Quantum Academy, Shenzhen 518048, China*
[d] *College of Physics, Nanjing University of Aeronautics and Astronautics, Nanjing 211106, China*
[e] *School of Physical Sciences, Great Bay University and Great Bay Institute for Advanced Study, Dongguan 523000, China*
[f] *International Center for Quantum Materials, School of Physics, Peking University, Beijing 100871 China*
[g] *Interdisciplinary Institute of Light-Element Quantum Materials and Research Center for Light-Element Advanced Materials, Peking University, Beijing 100871, China*
[h] *Shenzhen Institute of Advanced Technology, Chinese Academy of Sciences, Shenzhen 518055, China*
[i] *School of Physics and Electronics, Henan University, Kaifeng 475004, China*

ARTICLE INFO

Article history:
Received 7 February 2026
Revised 10 March 2026
Accepted 12 March 2026
Available online 15 March 2026

Keywords:
Triangular lattice
Geometric frustration
Molecular-brick chemical strategy
Structure-magnetic properties relationship
Crystal orbital Hamilton population

ABSTRACT

Equilateral triangular lattices (TLs) with antiferromagnetic interactions are ideal templates for inducing magnetic frustration, offering a platform to explore exotic quantum spin states that are crucial for advancing quantum science and technology. However, few examples meet these structural criteria, and even fewer realize these fascinating physical properties. We report four novel equilateral TL magnets realized through a crystal-symmetry-protected molecular-brick strategy. By deliberately selecting a high-symmetry nonmagnetic structural template and incorporating magnetic molecular building blocks, magnetic ions are geometrically constrained by three-fold rotational symmetry within the *a-b* plane, enforcing an ideal equilateral TL and turning on magnetism in a nonmagnetic structural template. Magnetic susceptibility and specific heat measurements reveal a long-range magnetic ordering in $BaCoBe_2(BO_3)_2F_2$ around 180 mK, while $BaNiBe_2(BO_3)_2F_2$ remains disordered at 140 mK. Furthermore, crystal orbital Hamilton population analysis shows that different molecular bricks exhibit distinct bonding characteristics, resulting in diverse magnetic properties. Our results demonstrate that the molecular-brick chemical strategy offers valuable insights into the investigation of geometrically frustrated magnets.

© 2026 Published by Elsevier B.V. on behalf of Chinese Chemical Society and Institute of Materia Medica, Chinese Academy of Medical Sciences.

Geometrically frustrated magnets (GFMs) are pivotal in exploring exotic quantum magnetism due to the highly macroscopic degeneracy and strong quantum fluctuations [1,2]. Geometric frustration—arising from lattice geometry and competing antiferromagnetic (AFM) interactions—gives rise to a variety of novel quantum phenomena, including quantum spin liquid (QSL) [3], spin supersolid [4], spin nematic state [5], and magnetization plateau [6]. Such exotic behaviors have been discovered not only in two-dimensional (2D) frustrated lattices, such as the triangular and Kagome lattices, but also in three-dimensional (3D) frustrated frameworks, including the pyrochlore [7], hyperkagome [8], and trillium lattices [9], which have enabled a more profound understanding of exotic physical properties and potential applications in quantum computing [10]. As one of the typical GFMs, equilateral triangular lattice antiferromagnets (ETLAFs) are proposed to have a QSL state in theory [11]. Subsequently, emergent quantum phenomena, including QSL and quantum phase transitions, have been experimentally observed in the aforementioned TL magnetic system [12]. For example, 1/3, 2/3, *etc.* magnetization plateaus have been discovered in 3d transition metal-contained materials, such as Cs_2CuBr_4 [13], $Ba_3CoSb_2O_9$ [14], and $Ba_3NiSb_2O_9$ [15]. Due to significant quantum fluctuations, TL magnets with small quantum

* Corresponding authors.
E-mail addresses: yaoqiushi@nuaa.edu.cn (Q. Yao), guos@sustech.edu.cn (S. Guo).

https://doi.org/10.1016/j.cclet.2026.112623
1001-8417/© 2026 Published by Elsevier B.V. on behalf of Chinese Chemical Society and Institute of Materia Medica, Chinese Academy of Medical Sciences.

spin numbers, such as $YbMgGaO_4$ (pseudospin $S_{eff} = 1/2$) [16], and $Ba_3NiSb_2O_9$ ($S = 1$) [17,18] have been proposed as QSL candidates. A Co^{2+}-based ETLAF, $Na_2BaCo(PO_4)_2$, was recently identified as a spin supersolid candidate with a giant magnetocaloric effect (MCE), bridging unconventional quantum phenomena with potential applications in millikelvin-level magnetic refrigeration [4].

However, the fabrication of 2D ETLAFs is hindered by structural disorder, lattice distortion, and interlayer correlations. For instance, $YbMgGaO_4$ was first proposed as a QSL candidate, and further studies show that the interplay of Mg^{2+}/Ga^{3+} site disorder remains debatable [19]. From the structural point of view, crystal symmetries, coordination environments, and polyhedral connectivity are crucial components of material structure. Materials exhibit distinct magnetism across different structural dimensions, arising from the combined influence of exchange interactions, crystal electric field (CEF) effects, spin-orbit coupling (SOC), and quantum fluctuation [20–22]. Hence, designing ETLAFs free from structural disorder and establishing these ideas in real materials remains exciting and challenging for the chemistry and material science communities.

During our previous investigation, we designed a series of deep-UV optical materials, $BaM(II)Be_2(BO_3)_2F_2$ (M = Zn, Mg, Ca, Cd) [23–25], derived from the structural motif of $Sr_2Be_2B_2O_7$ (SBBO, $P\bar{6}c2$). Given the high transparency in the deep-UV, d^0 or d^{10} transition metals were selected to maintain wide band gaps and optical transparency in the deep-UV region. High crystallographic symmetry was not a prerequisite for achieving the targeted optical functionality. In contrast, the present study is motivated by an entirely different objective: The realization of an ideal equilateral TL capable of hosting geometrical magnetic frustration. When magnetic ions with unpaired electrons are introduced into the high-symmetry space group of SBBO-type motifs, it is not merely chemical substitution of similar cations but activating a new collective degree of freedom, spin, within a symmetry-protected lattice geometry. Herein, a molecular-brick chemical strategy is successfully applied to explore equilateral TL quantum magnets. It refers to a chemical design based on high-symmetry structural motifs with 3-fold or 6-fold rotation symmetry. The nonmagnetic BO_3 and BeO_3F units, along with nonmagnetic cations, act as building blocks, analogous to toy bricks, that link the magnetic centers to form a 2D frustrated magnetic lattice [26]. With all the above in mind, four novel equilateral TL magnets, $BaCoBe_2(BO_3)_2F_2$ (BCBF), $BaNiBe_2(BO_3)_2F_2$ (BNBF), $SrCoBe_2(BO_3)_2F_2$ (SCBF), and $SrNiBe_2(BO_3)_2F_2$ (SNBF), have been rationally designed *via* molecular-brick chemical strategy and synthesized by a high-temperature flux method. Given their structural similarities, we focused on the magnetism and specific heat studies of BCBF and BNBF as representative compounds. Easy-plane anisotropic magnetic characteristics are found in all four materials with no detectable magnetic ordering down to 1.8 K. Further alternating current (AC) magnetic susceptibilities and thermodynamic measurements confirmed the long-range magnetic ordering (LRO) for the BCBF (180 mK). Intriguingly, the LRO was ruled out in the case of BNBF down to the millikelvin range based on the direct current (DC) magnetic susceptibilities (400 mK) and specific heat (140 mK) measurements. The different magnetic pictures of these TL magnets primarily arise from the intricate interplay between the CEF, SOC, electron configurations of magnetic ions, and the competition among different exchange interactions. Our results indicate that the newly developed equilateral TL 3d transition metal-based fluorides are promising candidates for exploring frustrated magnetism.

The functionalities and research appeal of materials primarily arise from the fundamental characteristics of their crystal structures. Initially, a classical deep-UV nonlinear optical (NLO) material, SBBO [27], was selected as a structural template for the unique crystal symmetry based on the molecular-brick strategy (Fig. 1A). Due to its noncentrosymmetric (NCS) space group ($P\bar{6}c2$) and the perfectly coplanar configuration of its BO_3 groups, SBBO has long been considered a promising NLO material for achieving deep-UV ($\lambda < 200$ nm) lasers through frequency doubling techniques [27,28]. In recent years, SBBO has been regarded as an excellent structural template for the development of novel NLO materials, such as $K_2Al_2B_2O_7$ [29], and $NaCaBe_2B_2O_6F$ [30]. Despite extensive exploration of SBBO in optical materials over the past decades, its potential to host highly symmetric magnetic sublattices has been largely overlooked. Structurally, two unique Sr atoms in the SBBO are fully fixed on the equilateral TL planes due to the six-fold rotation symmetry. This also makes SBBO an excellent template for exploring novel equilateral TL quantum magnets. Firstly, the high symmetry of the SBBO crystal structure can stabilize the equilateral TL. Next, magnetism can be systematically introduced into this TL by incorporating 3d transition metal ions such as Co^{2+} and Ni^{2+}, which possess relatively small quantum spin numbers. Our approach is fundamentally different from straightforward cation replacement. The targeted introduction of magnetic ions is guided by crystallographic symmetry constraints rather than by simple chemical similarity. Finally, the structural template can be further optimized by introducing complementary cations (*e.g.*, Ba^{2+}) and anions (*e.g.*, F^-) to maintain electroneutrality. Building on these ideas, a series of novel TL magnets, BCBF, BNBF, SCBF, and SNBF, has been designed using the SBBO structural template and a molecular-brick chemical strategy. We believe our work not only expands the application scope of SBBO-type templates but also provides a general strategy for designing new quantum magnetic materials based on well-established structural motifs. These materials were synthesized in millimeter-sized single-crystal form *via* a high-temperature flux method (Fig. 1B). Then, their crystal structures were determined by single-crystal X-ray diffraction (SC-XRD), revealing 2D structural features similar to those of the mother structure of SBBO. Considering the isomorphic structure of BCBF, BNBF, SCBF, and SNBF, the crystal structure of BNBF, refined at 100 K, is discussed here as a representative (Figs. 1C and D). It is crystallized in a trigonal crystal system with a centrosymmetric (CS) space group $P\bar{3}$ (No. 147). Each atom has only one unique position in the asymmetric unit of BNBF. Their coordination environments are depicted in Fig. S1 (Supporting information). Notably, the small sizes of BO_3 and BeO_3F make them good linkages for constructing the TL within the crystal structure. For the magnetic part, the Ni^{2+} ions are in NiO_6 octahedral form with $d(Ni{-}O) = 2.09$ Å. The NiO_6 octahedra are bridged with BO_3 triangles and BeO_3F tetrahedra *via* corner-sharing, further constructing a Ni-based TL in the *a*-*b* plane. The neighboring TLs are well-separated by non-magnetic BaO_6F_6 polyhedra with the nearest inter-plane distance ($d_{inter} = 7.62$ Å) significantly larger than that in the TL planes ($d_{intra} = 4.58$ Å) for BNBF (Fig. 1E). The magnetic TLs follow an A-A-A eclipsed stacking form along the crystallographic *c*-axis for all four materials. Scanning transmission electron microscopy (STEM) characterization further corroborates the structural features determined by SC-XRD. A BNBF sample with approximate dimensions of $5 \times 5 \times 2$ μm^3 and a thickness below 100 nm is prepared for analysis (Figs. 1F and G). Within the (210) plane, an enlarged High-Angle Annular Dark-Field (HAADF)-STEM image of BNBF was directly compared with its corresponding structural model and simulated image. The excellent agreement between experimental observations and theoretical projections further validates the accuracy of the structural model (Figs. 1H and I). Further structural analysis, such as the potential O/F disorder, will rely on neutron scattering experiments using ^{11}B-based crystals. Similarly, the magnetic framework, crystal structure, and polyhedral view of BCBF, SCBF, and SNBF are presented in Figs. S2-S4 (Supporting information), respectively. Additionally, the structural information for the above materials is pro-

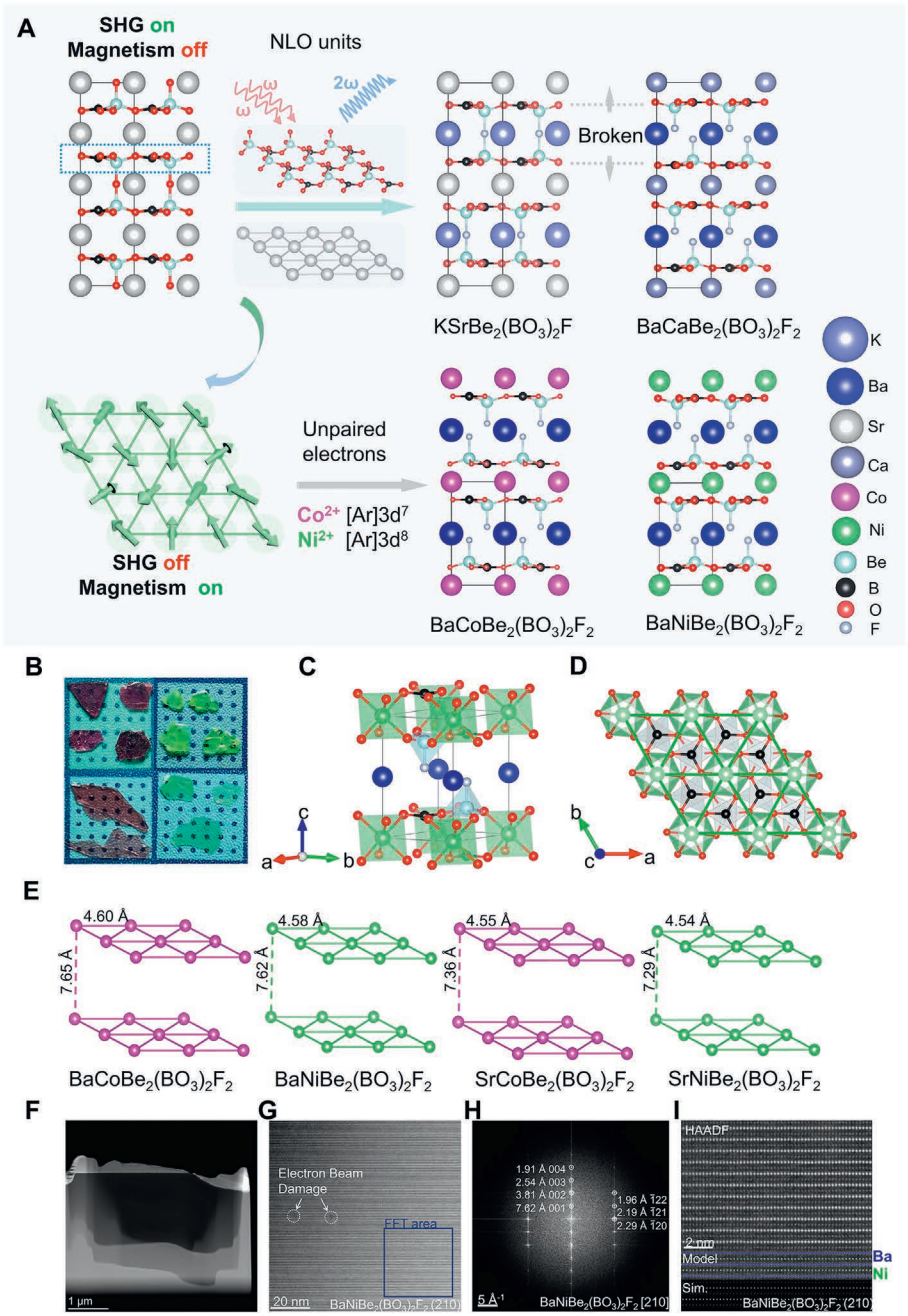


Fig. 1. Structural design and validation. (A) Structural evolution from SBBO to BNBF and BCBF. (B) The topography of single crystals of BCBF (upper left), BNBF (upper right), SCBF (bottom left), and SNBF (bottom right). (C) Unit cell of BNBF. (D) The triangular layer of magnetic NiO_6 octahedral in the *a*-*b* plane. (E) The magnetic frameworks with different interplane and intraplane distances. (F) STEM sample topography. (G) HAADF-STEM image of the BNBF (210) crystal plane, with annotated regions showing electron beam damage and the selected area for FFT pattern analysis. (H) FFT pattern of the BNBF [210] crystal orientation from (G). (I) Enlarged HAADF-STEM image of BNBF, along with its corresponding structural model and simulated image.

vided in Tables S1 and S2 (Supporting information). The ultraviolet absorption edges of BCBF, BNBF, SCBF, and SNBF are approximately 242, 217, 231, and 212 nm, respectively (Fig. S7 in Supporting information), indicating insulating behavior for these materials.

Given the differences in electron configuration (Fig. 2A), BCBF and BNBF were selected for detailed characterization of magnetic properties. For the bulk magnetic properties, averaged (ave) DC magnetic susceptibilities (χ) of BCBF were measured based on a polycrystalline sample with the applied field $B = 0.2$ T over the temperature range of 1.8-300 K. The inverse magnetic susceptibility (χ^{-1}) *versus* the T curve could be fitted well by the Curie-Weiss (CW) law $1/\chi = (T - \Theta)/C$ at both high-temperature (HT) and low-temperature (LT) regimes. The values for the effective moment μ_{eff}, Curie constant C, and Weiss temperature Θ have been summarized in Table S3 (Supporting information). From the standard CW fitting in the HT regime (100-300 K, Fig. 2B), the substantial negative CW temperature $\Theta_{ave} = -43.39$ K could be obtained, and the effective moment $\mu_{eff} = 5.70\ \mu_B/Co^{2+}$ is much larger than that from the spin-only value $g\sqrt{S(S+1)} = 3.87$ for $S = 3/2$ with $g = 2$, which suggests large orbital contributions in BCBF. Given that Co^{2+} in BCBF adopts octahedral coordination with a $(t_{2g})^5(e_g)^2$ configuration, corresponding to a spin state of $S = 3/2$ and an effective orbital moment $L = 1$. Specifically, when the strength of SOC is sufficiently large, it effectively couples the orbital (L) and spin

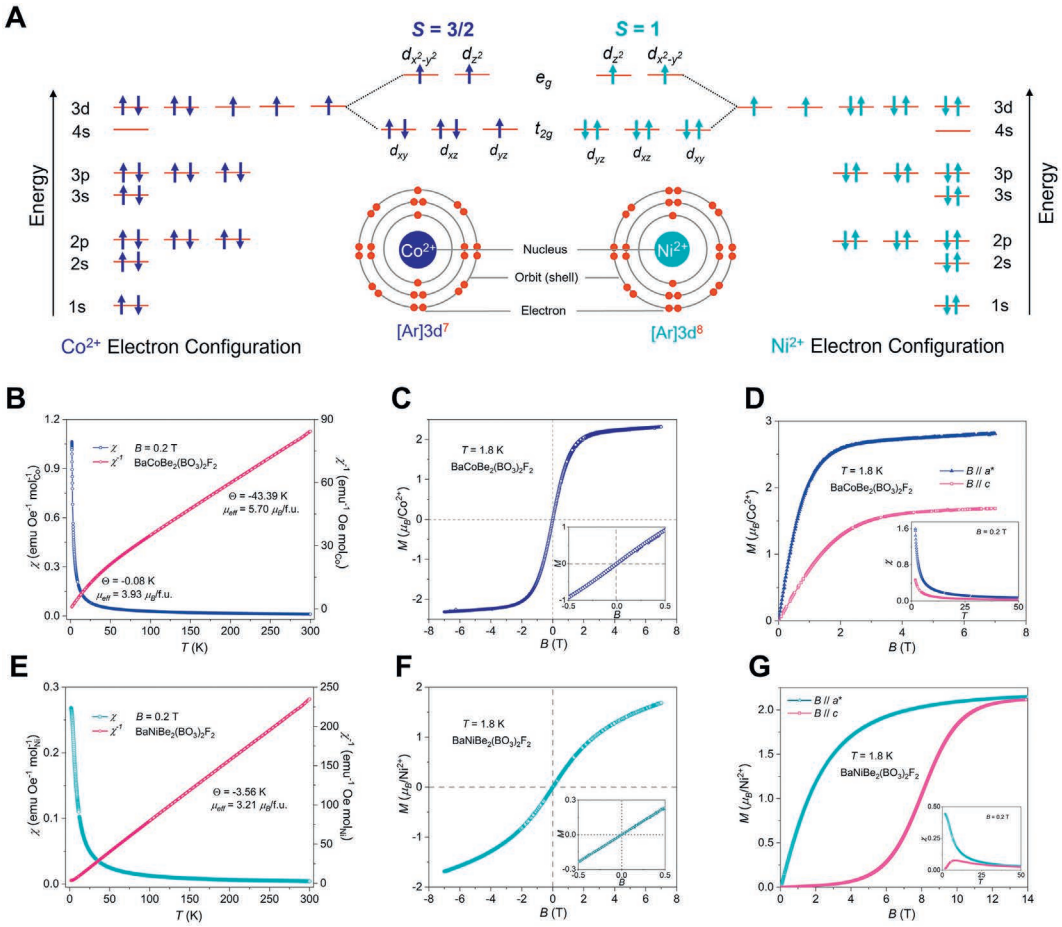


Fig. 2. Electron configurations, isotropic, and anisotropic magnetic properties. (A) The electron configurations of Co^{2+} and Ni^{2+}. Temperature-dependent magnetic susceptibility χ, and inverse susceptibility, $1/\chi$, with applied field $B = 0.2$ T of polycrystalline samples (B) BCBF and (E) BNBF. Magnetization $M(B)$ of polycrystalline samples (C) BCBF and (F) BNBF measured at 1.8 K. The insets C and F show $M(B)$ curve zoom in -0.5 T to 0.5 T. Magnetization $M(B)$ along crystallographic a^* and c axes of a single crystal of (D) BCBF and (G) BNBF at 1.8 K. The insets in (D) and (G) show temperature-dependent magnetic susceptibility χ with applied field $B = 0.2$ T along crystallographic a^* and c axes of single crystals of BCBF and BNBF, respectively.

(S) angular momentum into a new quantum number, the total angular momentum J, $J = L + S$. Under strong SOC, the energy levels of electrons are split not primarily by their original spin and orbital components but rather by the new J component. For the given Co^{2+} configuration, with $L = 1$ and $S = 3/2$, SOC can lead to different J states; however, in an octahedral crystal-field environment, the lowest-energy state typically corresponds to effective pseudospin-1/2. It can be treated as an effective pseudospin-1/2 Kramers doublet TL magnet at low temperatures due to the interplay of SOC and CEF (Fig. 2A) [31]. Linear LT (1.8-20 K) CW fitting gives a small negative CW temperature $\Theta_{ave} = -0.08$ K and $\mu_{eff} = 3.93\ \mu_B/Co^{2+}$. The small negative Θ_{ave} from LT CW fitting implies weak AFM interactions in BCBF. The slope change in the $\chi^{-1}(T)$ curve of BCBF reflects a temperature-driven crossover, from a high-temperature regime where multiple CEF levels contribute to the effective moment, to a low-temperature regime dominated by the lowest Kramers doublet. The hysteresis loop was not observed in the isothermal magnetization $M(B)$ curve of BCBF (Fig. 2C). To further reveal the anisotropic magnetic behaviors of BCBF, the isothermal magnetization $M(B)$ curves are measured at 1.8 K of a single crystal with the magnetic field along the crystallographic a^* and c axes of BCBF (Fig. 2D). Field-dependent magnetizations are nearly isotropic for the field in the a-b plane (Fig. S9B in Supporting information) with an approximately 2.81 μ_B/Co^{2+} saturation moment along the crystallographic a^* axis (Fig. 2D), which is significantly larger than that of $B//c$ (1.69 μ_B/Co^{2+}). From the $\chi(T)$ curves of BCBF with $B//c$ and $B//a^*$, easy-plane magnetic anisotropy with $\chi_{a^*} > \chi_c$ could be found in the magnetic susceptibility curves of BCBF in the LT range (inset of Fig. 2D and Fig. S9A in Supporting information). A similar easy-plane magnetic anisotropy is also observed in other Co-based TL magnets [32].

With Ni^{2+} ([Ar]3d^8) as the magnetic ion, the integer spin $S = 1$ TL system is likely to exhibit distinct magnetic behavior (Fig. 2A). The temperature dependencies of χ and its inverse, χ^{-1}, for BNBF are displayed in Fig. 2E. Upon cooling, no clear, sharp peak is observed in the $\chi(T)$ curve above 1.8 K based on a polycrystalline sample. CW fitting is performed based on the linear behavior of χ^{-1} above 100 K, which gives $\mu_{eff} = 3.21\ \mu_B/Ni^{2+}$ and $\Theta_{ave} = -3.56$ K. The value of μ_{eff} for BNBF is similar to other Ni^{2+}-based frustrated magnets [33] and slightly larger than the ideal value of 2.83 μ_B expected for $S = 1$. The negative CW temperature implies the predominant AFM coupling in the magnetic Ni^{2+} of BNBF. No hysteresis loop was observed in the $M(B)$ curve of BNBF (Fig. 2F). Examining the $M(B)$ curves along diverse directions reveals that magnetization is virtually indistinguishable along the a and a^* axes (Fig. S9D in Supporting information). As seen from the $M(B)$ data at a higher field along the direction of a^*-axis, the magnetic moment begins to flatten around 10 T, and $M_{max} = 2.14\ \mu_B/Ni^{2+}$ at 14 T (Fig. 2G). Similar to BCBF, the easy-plane anisotropic magnetic behavior is found for BNBF. Interestingly, as shown in Fig. 2G inset and Fig. S9C (Supporting information), no sharp anomaly could be observed with fields in two orientations ($B//a^*$ and $B//c$), but a broad

hump can be observed in the $\chi(T)$ curve with the maximum value around $T_{max} = 8.26$ K with $B//c$. It is worth mentioning that the LRO was not captured down to 1.8 K with a magnetic field along all three directions, which suggests the potentially interesting, frustrated magnetism in BNBF. The broad maximum at $T_{max} = 8.26$ K for $B//c$ is most likely associated with the development of short-range AFM correlations. In BNBF, the Ni^{2+} ions interact antiferromagnetically on a TL, where geometrical frustration suppresses LRO and favors strong short-range spin correlations, which naturally give rise to such broad maxima. Similar $\chi(T)$ humps are commonly observed in other Ni^{2+}-based TL magnets, including 6HB-$Ba_3NiSb_2O_9$ and $NiGa_2S_4$ [34]. Another possible contribution comes from the single-ion anisotropy of $S = 1$ Ni^{2+}. A sizable easy-plane ($D > 0$) anisotropy can split the $S = 1$ triplet into a nonmagnetic singlet ground state and a doublet excited state. This mechanism suppresses the magnetic response at low temperatures and naturally produces a broad $\chi(T)$ maximum, as observed in systems such as the one-dimensional Ni^{2+}-based compound $NiCl_2$-4SC$(NH_2)_2$ [35]. To conclusively determine the magnetic ground state, further measurements, such as neutron scattering or electron paramagnetic resonance, will be highly valuable, as they can distinguish between short-range order, singlet-based magnetism, or more unconventional frustrated states.

To further elucidate the magnetic ground states of $BaMBe_2(BO_3)_2F_2$ (M = Co, Ni), the AC susceptibility (χ'), DC susceptibility, and specific heat (C_p) were measured down to millikelvin temperatures. As depicted in Fig. 3A, the zero-field C_p manifests a λ-like peak around 180 mK for BCBF, which indicates an LRO and aligns well with the sharp peak around 180 mK in the AC susceptibility curve (Fig. 3G). For the thermodynamics study, zero-field and field-dependent specific heat for both materials were measured with $B//c$. Considering the absence of an isostructural non-magnetic reference compound, a two-Debye model fitting was applied to estimate the phonon contribution to the specific heat of BCBF (see Supporting information for details). It appears that the primary contribution to magnetic entropy during 0 T conditions comes from the integral of magnetic specific heat C_m/T below 4 K. Magnetic entropy S_m is estimated by integrating the magnetic specific heat C_m/T, approaching $R\ln 2$ at 4 K in zero magnetic field, suggesting an effective total angular momentum pseudospin-1/2 system for BCBF (Figs. 3B and C). When a small magnetic field, $B = 0.5$ T, is applied, the LRO is suppressed and shifts to higher temperatures with increasing the fields. This broad feature might be attributed to field-induced short-range spin correlations or a Schottky-like contribution arising from Zeeman splitting, which is also observed in other Co^{2+}-based TL antiferromagnets [36,37]. Considering the application of $Na_2BaCo(PO_4)_2$ in adiabatic demagnetization refrigeration (ADR), we further investigated the MCE of a structurally related cobalt-based compound, BCBF. Our calculations show that BCBF exhibits a substantial magnetic entropy change ($-\Delta S_m$) of 15.35 J kg^{-1} K^{-1} near 0.87 K under an applied magnetic field of 3 T (Fig. S11 in Suppoorting information), highlighting its promise for ADR application in the sub-Kelvin temperature regime.

Interestingly, very different magnetic features are observed in BNBF with the integer spin number $S = 1$. As shown in Fig. 3D, the zero-field heat capacity $C_p(T)$ displays a broad hump centered around 4.65 K, with no indication of LRO down to 140 mK. The broad hump in Fig. 3D changed with external magnetic fields, which might be related to the short-range correlation or the Schottky-like contributions. Further experiments, such as muon spin rotation (μSR), nuclear magnetic resonance (NMR), and inelastic neutron scattering, will help to map the physical picture of these two Ni-based TL antiferromagnets. To study the evolution of this broad hump, we examine the variation of C_m/T between 1.8 K and 30 K under different magnetic fields, displayed in Fig. 3E. C_m was obtained by subtracting the phonon contributions of BNBF from the modified Debye model fitting (Fig. 3D). A closer examination of the $C_m(T)$ data under varying magnetic fields reveals a broad anomaly at 3.65 K for $B = 0$ T, which shifts to a lower temperature as the magnetic field increases. The calculated magnetic entropy, S_m, was evaluated *via* $S_m = \int_0^T (C_m/T)dT$ (see Supporting information for details). At $B = 0$ T, the S_m of BNBF equals 8.52 J mol^{-1} K^{-1} (Fig. 3F), closely approximating the constant $R\ln(2S+1)$ value for an $S = 1$ system. No frequency-dependent behavior was observed around the broad anomaly at 3.65 K in the specific heat or $T_{max} = 8.26$ K in the $\chi(T)$ curve with $B \perp c$ (Fig. 3H). The zero-field-cooling (ZFC) and field-cooling (FC) magnetic susceptibility along the *a* axis reveal no bifurcation down to 0.4 K (Fig. 3I), further excluding the presence of spin freezing or ferromagnetic ordering down to 0.4 K. To quantify the magnetic frustration, the spin frustration of BNBF was evaluated *via* $f = |\Theta|/T_N$, which gives a minimum $f = 25$. Although the substantial frustration parameter suggests geometrical frustration and suppressed LRO, definitive confirmation must await more direct probing methods.

From the viewpoint of structural chemistry, the geometries of triangles, stacking forms of TL layers, polyhedral connectivity of magnetic ions, and spacer/bridging units are critical components for fabricating TL materials, directly influencing their magnetic properties. Geometrically, triangles can be classified into several common types based on their angles and side lengths (Fig. 4A). In equilateral TLs, the equivalence of nearest-neighbor (NN) spin interactions leads to a highly degenerate classical ground state, making geometrical frustration inherent to the system. In quantum magnets, this frustration, together with quantum fluctuations, can even stabilize exotic disordered states such as QSL. By contrast, lattice distortions break the symmetry of the triangular geometry, introducing inequivalent spin couplings. This partial lifting of the ground-state degeneracy tends to relieve frustration and often favors the development of LRO. Typically, the stacking patterns of TL could be classified based on arrangements of the neighboring TL layers, generating different fashions such as AAA, ABAB, AABB, and ABCABC stacking forms (Fig. 4B). Depending on the bridging units (BO_3, PO_4, NbO_6, and SbO_6) and diverse polyhedral connectivity (corner-, edge-, or face-sharing), the distance between magnetic ions in the TL (d_{intra}), therefore, varies across materials (Fig. 4C). Notably, the distance of magnetic ions between the adjacent TL (d_{inter}), which is closely associated with NN interlayer exchange couplings (J_1), could be tuned by spacers such as nonmagnetic cations and bridging units (Fig. 4D). Recently, Jin, *et al.* reported a pyroxene-based quantum magnet and elucidated the important role of center cations' electron configurations in magnetic exchange interactions [38].

To elucidate the structure-properties relationship, physical properties and structural features of typical Co- and Ni-based TL oxides are selected and summarized in Table 1. It is worth mentioning that the quantity and spatial size of spacers and bridging units are crucial for regulating intralayer and interlayer distances. The d_{inter} of $Ba_3CoNb_2O_9$ [39], $Na_2BaCo(VO_4)_2$ [40], $Na_2BaCo(PO_4)_2$, and BCBF are found in the range of 7.01-7.65 Å. As a particular example, the number of spacers in $Ba_8CoNb_6O_{24}$ is significantly more than that of other materials in Table 1, resulting in a large interlayer distance (d_{inter}) of 18.90 Å. In the case of Ag_2CoO_2 and Ag_2NiO_2, the octahedral CoO_6 or NiO_6 are connected *via* simple edge-sharing O atoms to construct TL layers along the *c* axis. The close NN distance $d_{intra} = 2.85$-2.92 Å implies a relatively large NN coupling J_1 and further explains LRO at relatively high temperatures ($T_N = 17.5$ K for Ag_2CoO_2 [41] and $T_N = 56$ K for Ag_2NiO_2 [42]). With the relatively large PO_4 and NbO_6 building blocks as bridging units in the TL plane, the d_{intra} is usually larger than 4 Å, increasing the magnetic exchange coupling paths

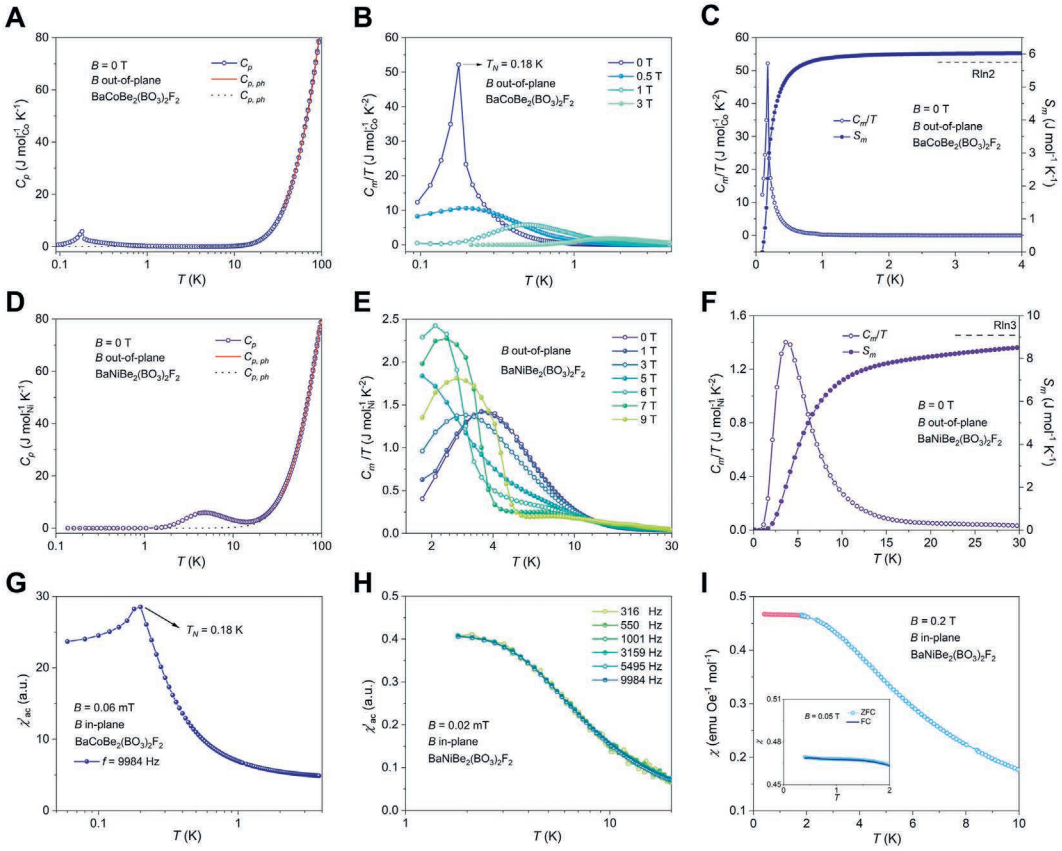


Fig. 3. Ultralow-temperature thermodynamics and magnetic susceptibility. (A, D) Zero-field specific heat, C_p, of BCBF (A, blue circles) and BNBF (D, purple circles) from 100 K down to ultralow temperature. The red line is the phonon contributions fit to two Debye mode between 35 K and 100 K in the zero field. The black dot line represents data extrapolated using the Debye model below 35 K. (B, E) Magnetic specific heat over temperature, C_m/T, for BCBF and BNBF, was measured under several magnetic fields. The magnetic entropies (S_m) *versus* temperature by integrating C_m/T of (C) BCBF and (F) BNBF. AC magnetic susceptibilities χ'_{ac} of (G) BCBF and (H) BNBF. (I) The $\chi(T)$ curve with an applied field of $B = 0.2$ T along the crystallographic *a* axis of a single crystal for BNBF. The blue cycles of the curve represent magnetic susceptibility data (1.8-10 K), and the pink cycles represent magnetic susceptibility data measured using a ^{3}He system (0.4-2 K). The inset shows the $\chi(T)$ curve (0.4-2 K) under a magnetic field of 0.05 T.

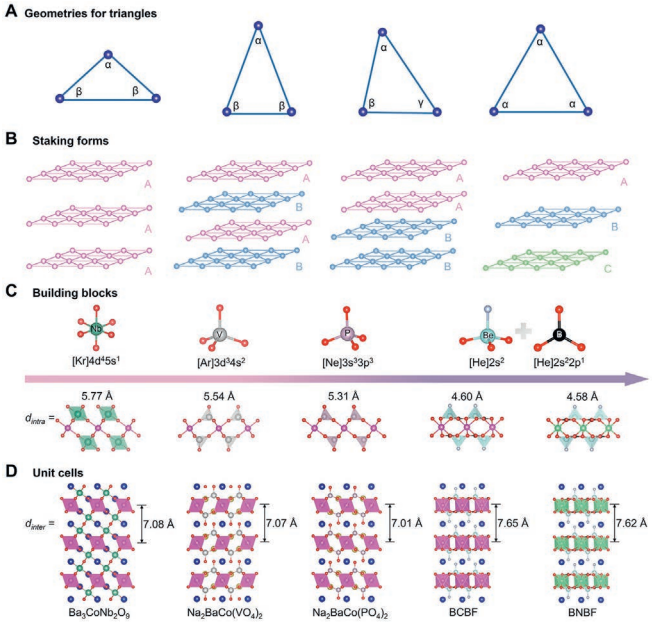


Fig. 4. Molecular-brick chemical strategies for equilateral TL materials. (A) Various triangle geometries (isosceles, scalene, and equilateral). (B) Typical stacking forms of TL layers in different fashions. (C) Bridging blocks with diverse spatial sizes to connect the magnetic ions in the TL layers. (D) The unit cell of typical TL materials with different types and quantities of spacers.

and weakening the NN magnetic exchange couplings. Here, we introduce the $R_{TL} = d_{inter}/d_{intra}$ ratio to evaluate the dimensionality of TL lattice materials. $Na_2BaCo(PO_4)_2$ [36] and its Ni-version are typical AAA stacking forms with the $d_{inter} = 7.01$ Å extensively larger than that of $d_{intra} = 5.32$ Å. The R_{TL} values of BCBF and BNBF were also evaluated. Both compounds exhibit relatively large R_{TL} values compared with TL magnets listed in Table 1, highlighting their 2D structural feature. Recent results revealed the spin supersolid state in the $Na_2BaCo(PO_4)_2$ [4] and Bose-Einstein condensation of the two-magnon bound state in $Na_2BaNi(PO_4)_2$ [6]. In the case of $Ba_8CoNb_6O_{24}$, the d_{inter} is as large as 18.90 Å with $R_{TL} = 3.26$, making it a truly TL magnet free of magnetic exchange couplings between the TL layers. Preliminary results from polycrystalline samples rule out the LRO down to 28 mK and suggest promising quantum states for $Ba_8CoNb_6O_{24}$ [43–45]. As an exception to regular TL materials, the magnetic ions are arranged in an AA-BB-CC stacking pattern in the crystal structure of Ba_2NiTeO_6 [46]. The Ni^{2+}-Ni^{2+} distances with first-, second-, and third-neighbors are comparable, so it is considered a buckled honeycomb lattice other than a conventional 2D TL magnet.

Benefiting from the compact spatial size of BO_3 and BeO_3F units, our newly discovered materials, therefore, exhibit relatively short magnetic distances in the TL plane, measured as 4.60 Å in BCBF, 4.58 Å in BNBF, 4.55 Å in SCBF, and 4.54 Å in SNBF, respectively. Hence, these four materials are successful examples of maintaining the balance between d_{intra} and d_{inter}. In the case of BCBF, the ultralow-temperature LRO (180 mK) implies magnetic frustration. Strikingly, the absence of LRO down to even 140 mK gives

Table 1
Comparison of structural features and magnetic properties of typical Co- or Ni-based TL materials.

Compound	Space group	Stacking fashion	d_{intra} (Å)	d_{inter} (Å)	R_{TL}	d_{inter}/d_{intra}	Magnetic properties
Ag_2CoO_2 [41]	$P\bar{3}m1$	A-A-A	2.85	8.60	3.02		AFM transition at $T_N = 17.5$ K
Ag_2NiO_2 [42]	$R\bar{3}m$	A-B-C	2.92	8.01	2.74		AFM transition at $T_N = 56$ K
$Na_2BaCo(PO_4)_2$ [4,36,37,47]	$P\bar{3}m1$	A-A-A	5.32	7.01	1.32		Easy-axis magnetic anisotropy, AFM ordering at $T_N = 0.15$ K, spin supersolid candidate
$Na_2BaNi(PO_4)_2$ [5,48,49]	$P\bar{3}$	A-A-A	5.28	6.96	1.32		Easy-axis magnetic anisotropy, magnetic ordering at $T_N = 0.43$ K, spin nematic phase
$Ba_3CoNb_2O_9$ [39]	$P\bar{3}m1$	A-A-A	5.77	7.08	1.23		Possible easy-axis anisotropy, two-step transitions at $T_{N2} = 1.36$ K and $T_{N1} = 1.10$ K
$Ba_3NiNb_2O_9$ [50]	$P\bar{3}m1$	A-A-A	5.76	7.07	1.23		Up-up-down phase and multiferroicity
$Ba_3CoSb_2O_9$ [51–53]	$P6_3/mmc$	A-A-A	5.86	7.23	1.23		Easy-axis magnetic anisotropy, successive magnetic phase transitions with an up-up-down phase stabilized even at 27 mK
6H-A $Ba_3NiSb_2O_9$ [17,51]	$P6_3/mmc$	A-A-A	5.84	7.20	1.23		AFM transition at 13.5 K
6H-B $Ba_3NiSb_2O_9$ [17]	$P6_3mc$	A-B-A-B	5.79	7.14	1.23		Absence of magnetic order down to 0.35 K
$Ba_8CoNb_6O_{24}$ [43–45]	$P\bar{3}m1$	A-A-A	5.79	18.90	3.26		Absence of LRO down to 0.028 K
$SrCoBe_2(BO_3)_2F_2$*	$P\bar{3}$	A-A-A	4.55	7.36	1.62		Easy-plane magnetic anisotropy, absence of LRO down to 1.8 K
$SrNiBe_2(BO_3)_2F_2$*	$P\bar{3}$	A-A-A	4.54	7.29	1.61		Easy-plane magnetic anisotropy, absence of LRO down to 1.8 K
$BaCoBe_2(BO_3)_2F_2$*	$P\bar{3}$	A-A-A	4.60	7.65	1.66		Easy-plane magnetic anisotropy, magnetic ordered around 0.18 K
$BaNiBe_2(BO_3)_2F_2$*	$P\bar{3}$	A-A-A	4.58	7.62	1.66		Easy-plane magnetic anisotropy, absence of LRO down to 0.05 K

d_{intra}: The distance between the nearest-neighbor magnetic ions in magnetic layers;
d_{inter}: The distance between the magnetic layers.
* This work.

a frustration index $f > 25$, making BNBF an ideal TL material for further interest in exotic quantum spin states. Due to their similar structural features, the magnetism of SCBF and SNBF closely resembles that of the BCBF and BNBF, respectively. The negative CW temperature $\Theta_{ave} = -0.92$ K, inferred from the LT CW fitting of SCBF, implies weak magnetic interactions (Fig. S10A in Supporting information). In contrast, the relatively larger CW temperature ($\Theta_{ave} = -1.32$ K) of SNBF suggests that AFM interactions dominate in SNBF (Fig. S10B in Supporting information). As shown in Figs. S10C and D (Supporting information), the magnetic hysteresis loop, typically associated with ferromagnetic behavior, is absent in the $M(B)$ curves for both SCBF and SNBF. Additionally, easy-plane magnetic anisotropy was found for both SCBF and SNBF (Figs. S10E and F in Supporting information), consistent with the magnetic behaviors of BCBF and BNBF. The investigation of ultralow-temperature magnetic and thermodynamic properties of SCBF and SNBF is ongoing, and the results will be presented in our upcoming paper.

To uncover the role of molecular-bricks, which connect magnetic atoms to form a TL, we carried out a comprehensive total energy and chemical bonding analysis using crystal orbital Hamilton populations (COHP) [54]. As shown in Fig. S12A (Supporting information), for $Ba_3CoNb_2O_9$, $Na_2BaCo(VO_4)_2$, $Na_2BaCo(PO_4)_2$, BCBF, and BNBF, we constructed nonmagnetic (NM) and four magnetic states, namely, ferromagnetic (FM), intralayer ferromagnetic while interlayer antiferromagnetic (AFM1, upper panel of Fig. S12A), intralayer antiferromagnetic interlayer ferromagnetic (AFM2, middle panel of Fig. S12A), intra- and interlayer antiferromagnetic (AFM3, down panel of Fig. S12A). Based on our calculations, on one hand, for BCBF and BNBF, comparable total energies (Fig. S12B and Table S4 in Supporting information) and similar COHP profiles (Figs. S12C and S15-S17 in Supporting information), especially the vanishing antibonding states in the vicinity of E_F, of all four magnetic configurations impede BCBF and BNBF from forming magnetic ordered states. On the other hand, for $Ba_3CoNb_2O_9$, it's interesting to notice that FM and AFM1 exhibit close resemblance, while AFM2 and AFM3 show analogous characteristics to each other, for both total energy (Fig. S12B and Table S4) and COHP (Fig. S12D in Supporting information). Notice that FM is intralayer FM and interlayer FM, labeled as intra-FM/inter-FM, AFM1 is intra-FM/inter-AFM, AFM2 is intra-AFM/inter-FM, AFM3 is intra-AFM/inter-AFM (Fig. S12A). With this said, we conclude that it is intra-AFM that plays the vital role in Co-NbO_6 bonding optimization and total energy lowering, while contributions from interlayer magnetic interactions are relatively tiny. Situation for $Na_2BaCo(VO_4)_2$ is quite similar to $Ba_3CoNb_2O_9$ (Figs. S12B and S13, Table S4 in Supporting information). For $Na_2BaCo(PO_4)_2$, the relatively high energy of AFM2 can also be ascribed to the Co-PO_4 antibonding states at E_F (Fig. S14 in Supporting information). As anticipated, AFM3, which is energetically most favorable, adopts the optimal bonding characters. As exemplified by the five compounds mentioned above, molecular-bricks facilitate a diverse range of bonding characteristics between the bridged magnetic atoms that form the TL, creating an ideal platform for investigating exotic quantum magnetic properties (see Supporting information for extended discussion).

Based on our abovementioned experimental and theoretical analysis of molecular-brick chemical strategy, key elements such as crystal symmetries, stacking patterns of TL layers, and the bridging units of magnetic ions are fundamental components of GFMs. While our present work retains the same structural motif as previous optical materials, it exhibits a fundamentally different conceptual framework, unique design criteria, and entirely new physical phenomena. These structural features are closely linked to the SOC, CEF, electron configurations, and magnetic interactions, *etc*., in GFMs, all of which significantly influence their intrinsic magnetism and quantum effects. To extend the structure evolution in the SBBO-type family, the structural comparison

and physical properties of typical SBBO-type materials are summarized in Fig. S5 and Table S5 (Supporting information), which verify the importance and tunability of this structural motif (Table S5). Our chemical strategy can also be extended to SBBO-type materials, thereby broadening the family of geometrically frustrated materials. Our molecular-brick chemical strategy can be extended to other magnetic ions with large quantum spin numbers, such as Mn^{2+} ($S=5/2$), as exemplified by the synthesized material $BaMnBe_2(BO_3)_2F_2$ in our lab, which holds great promise for future exploration of geometrical frustration and magnetic refrigeration. Moreover, our molecular-brick strategy can be adapted to various structural motifs involving TLs, as well as to other geometrically frustrated lattices, such as the Kagome and pyrochlore lattices, potentially inspiring the discovery of new GFMs and advancing research in the quantum realm.

In conclusion, the molecular-brick chemical strategy enables the design of equilateral TL magnets through a rational approach, combining crystal symmetry, coordination-chemistry principles, and magnetic frustration. We have shown the successful structural design and materials realization of four equilateral TL magnets, $BaMBe_2(BO_3)_2F_2$ and $SrMBe_2(BO_3)_2F_2$ (M = Co or Ni), based on the selected structural template from a classical NLO crystal. Structural analysis suggests fully ordered crystal structures for these four TL magnets, both chemically and positionally. The magnetic frameworks of the above materials exhibit equilateral TLs in the *a*-*b* plane, following an A-A-A staking pattern along the *c*-axis. Magnetic susceptibility and specific heat measurements indicate long-range magnetic ordering in BCBF at around 180 mK, whereas it is absent in BNBF down to 140 mK. Further theoretical analysis reveals that the bonding characteristics inherited from the building blocks are crucial in determining the magnetic spin states of the TL magnets. Our results suggest that BNBF is an $S=1$ TL material for exploring novel quantum magnetism. By repurposing structural motifs originally developed for deep-UV optical materials to geometrically frustrated materials, we demonstrate a pathway to convert nonmagnetic frameworks into geometrically frustrated magnets. This symmetry-driven chemical strategy goes beyond simple chemical substitution and opens new avenues for discovering novel quantum magnetic materials.

Declaration of competing interest

The authors declare no competing interest.

CRediT authorship contribution statement

Ruixin Guo: Writing – review & editing, Writing – original draft, Formal analysis, Data curation. **Jieming Sheng:** Writing – review & editing, Formal analysis. **Bowen Li:** Writing – review & editing, Writing – original draft, Data curation. **Kaizhen Guo:** Writing – original draft. **Wenjiao Yao:** Writing – review & editing, Writing – original draft. **Nan Zhao:** Writing – review & editing, Writing – original draft. **Jianqiao Wang:** Writing – review & editing. **Zhibin Qiu:** Writing – review & editing. **Bo Wen:** Writing – review & editing, Writing – original draft. **Shuang Jia:** Writing – review & editing, Funding acquisition. **Xiaoyang Wang:** Writing – review & editing, Writing – original draft. **Ping Wu:** Writing – review & editing. **Feng Yang:** Writing – review & editing. **Liusuo Wu:** Writing – review & editing, Writing – original draft, Funding acquisition. **Qiushi Yao:** Writing – review & editing, Writing – original draft, Methodology, Funding acquisition, Formal analysis, Conceptualization. **Shu Guo:** Writing – review & editing, Writing – original draft, Validation, Methodology, Funding acquisition, Formal analysis, Data curation, Conceptualization.

Acknowledgments

The authors acknowledge the financial support from the National Natural Science Foundation of China (Nos. 22205091, 12134020, and 12374146) and the National Key Research and Development Program of China (No. 2021YFA1400400). S. Guo thanks the Guangdong Pearl River Talent Plan (No. 2023QN10C793). Q. Yao thanks the support of the Startup Foundation of Nanjing University of Aeronautics and Astronautics (No. 1018-YAH23031). The work at Peking University was financially supported by the National Key Research and Development Program of China (No. 2021YFA1401902), National Natural Science Foundation of China (Nos. 12141002, 12225401), and CAS Interdisciplinary Innovation Team (No. JDTD-2019-08). The work at Great Bay University was financially supported by Guangdong Provincial Quantum Science Strategic Initiative (No. GDZX2401007). We thank Chengyi Guo for his assistance with retouching the figures. This article is also contributed to the Special Topics of Academic Papers at the 28th Annual Meeting of the China Association for Science and Technology.

Supplementary materials

Supplementary material associated with this article can be found, in the online version, at doi:10.1016/j.cclet.2026.112623.

References

[1] A. Ramirez, Annu. Rev. Mater. Sci. 24 (1994) 453–480.
[2] S.H. Lee, C. Broholm, W. Ratcliff, et al., Nature 418 (2002) 856–858.
[3] C. Broholm, R.J. Cava, S.A. Kivelson, et al., Science 367 (2020) 0668.
[4] J. Xiang, C. Zhang, Y. Gao, et al., Nature 625 (2024) 270–275.
[5] J. Sheng, J.W. Mei, L. Wang, et al., Nat. Mater. 24 (2025) 544–551.
[6] M. Takigawa, F. Mila, Magnetization plateaus, Springer, Berlin Heidelberg, 2010, pp. 241–267.
[7] J.S. Gardner, M.J.P. Gingras, J.E. Greedan, Rev. Mod. Phys. 82 (2010) 53–107.
[8] J.M. Hopkinson, S.V. Isakov, H.Y. Kee, et al., Phys. Rev. Lett. 99 (2007) 037201.
[9] M.G. Gonzalez, V. Noculak, A. Sharma, et al., Nat. Commun. 15 (2024) 7191.
[10] V. Lahtinen, J.K. Pachos, SciPost Phys. 3 (2017) 021.
[11] P.W. Anderson, Mater. Res. Bull. 8 (1973) 153–160.
[12] A.O. Scheie, E.A. Ghioldi, J. Xing, et al., Nat. Phys. 20 (2024) 74–81.
[13] T. Ono, H. Tanaka, H.A. Katori, et al., Phys. Rev. B 67 (2003) 104431.
[14] Y. Kamiya, L. Ge, T. Hong, et al., Nat. Commun. 9 (2018) 2666.
[15] Y. Shirata, H. Tanaka, T. Ono, et al., J. Phys. Soc. Jpn. 80 (2011) 093702.
[16] Y. Li, H. Liao, Z. Zhang, et al., Sci. Rep. 5 (2015) 16419.
[17] J.G. Cheng, G. Li, L. Balicas, et al., Phys. Rev. Lett. 107 (2011) 197204.
[18] C. Xu, F. Wang, Y. Qi, et al., Phys. Rev. Lett. 108 (2012) 087204.
[19] Z. Ma, J. Wang, Z.Y. Dong, et al., Phys. Rev. Lett. 120 (2018) 087201.
[20] B. Keimer, J.E. Moore, Nat. Phys. 13 (2017) 1045–1055.
[21] R. Cava, N. De Leon, W. Xie, Chem. Rev. 121 (2021) 2777–2779.
[22] R. Guo, R. Si, Z. Li, et al., Angew. Chem. Int. Ed. 63 (2024) e202410428.
[23] S. Guo, X. Jiang, M. Xia, et al., Inorg. Chem. 56 (2017) 11451–11454.
[24] R. Guo, X. Liu, C. Tao, et al., Dalton Trans. 50 (2021) 2138–2142.
[25] R. Guo, X. Jiang, S. Guo, et al., Inorg. Chem. 61 (2022) 7624–7630.
[26] H. Zhao, J. Song, S. Li, et al., Chin. Chem. Lett. 37 (2026) 111011.
[27] C. Chen, Y. Wang, B. Wu, et al., Nature 373 (1995) 322–324.
[28] M. Mutailipu, K.R. Poeppelmeier, S. Pan, Chem. Rev. 121 (2021) 1130–1202.
[29] C. Zhang, J. Wang, X. Cheng, et al., Opt. Mater. 23 (2003) 357–362.
[30] H. Huang, J. Yao, Z. Lin, et al., Chem. Mater. 23 (2011) 5457–5463.
[31] H. Liu, G. Khaliullin, Phys. Rev. B 97 (2018) 014407.
[32] Y. Kojima, M. Watanabe, N. Kurita, et al., Phys. Rev. B 98 (2018) 174406.
[33] M. Saito, M. Watanabe, N. Kurita, et al., Phys. Rev. B 100 (2019) 064417.
[34] D.E. MacLaughlin, S. Nakatsuji, Y. Nambu, et al., J. Phys. Conf. Ser. 145 (2009) 012040.
[35] N. Tsyrulin, C.D. Batista, V.S. Zapf, et al., J. Phys. Condens Mat. 25 (2013) 216008.
[36] R. Zhong, S. Guo, G. Xu, et al., Proc. Natl. Acad. Sci. U. S. A. 116 (2019) 14505–14510.
[37] N. Li, Q. Huang, X.Y. Yue, et al., Nat. Commun. 11 (2020) 4216.
[38] L. Jin, S. Peng, A.N. Rutherford, et al., Sci. Adv. 10 (2024) eadp4685.
[39] M. Lee, J. Hwang, E.S. Choi, et al., Phys. Rev. B 89 (2014) 104420.
[40] G. Nakayama, S. Hara, H. Sato, et al., J. Phys. Condens. Matter 25 (2013) 116003.
[41] H.K. Yoshida, S.E. Dissanayake, A.D. Christianson, et al., Phys. Rev. B 102 (2020) 024445.
[42] H. Yoshida, Y. Muraoka, T. Sörgel, et al., Phys. Rev. B 73 (2006) 020408.
[43] P.M. Mallinson, M.M.B. Allix, J.B. Claridge, et al., Angew. Chem. Int. Ed. 44 (2005) 7733–7736.
[44] R. Rawl, L. Ge, H. Agrawal, et al., Phys. Rev. B 95 (2017) 060412.
[45] Y. Cui, J. Dai, P. Zhou, et al., Phys. Rev. Mater. 2 (2018) 044403.

[46] S. Asai, M. Soda, K. Kasatani, et al., Phys. Rev. B 93 (2016) 024412.
[47] J. Sheng, L. Wang, A. Candini, et al., Proc. Natl. Acad. Sci. U. S. A. 119 (2022) e2211193119.
[48] F. Ding, Y. Ma, X. Gong, et al., Chin. Phys. B 30 (2021) 117505.
[49] N. Li, Q. Huang, A. Brassington, et al., Phys. Rev. B 104 (2021) 104403.
[50] J. Hwang, E.S. Choi, F. Ye, et al., Phys. Rev. Lett. 109 (2012) 257205.
[51] Y. Doi, Y. Hinatsu, K. Ohoyama, J. Phys. Condens. Matter 16 (2004) 8923–8935.
[52] Y. Shirata, H. Tanaka, A. Matsuo, et al., Phys. Rev. Lett. 108 (2012) 057205.
[53] H.D. Zhou, C. Xu, A.M. Hallas, et al., Phys. Rev. Lett. 109 (2012) 267206.
[54] R. Dronskowski, P.E. Bloechl, J. Phys. Chem. 97 (1993) 8617–8624.